Rock Mechanics and Rock Engineering (2023) 56:9085–9098
https://doi.org/10.1007/s00603-023-03508-8

ORIGINAL PAPER

Permeability–Friction Relationships for Propped Fractures in Shale

Jiayi Yu[1] · Jiehao Wang[2] · Yan Li[2] · Amr El-Fayoumi[2] · Ruiting Wu[2] · Xiaolong Liu[2] · Peggy Rijken[2] · Andrew P. Rathbun[2] · Derek Elsworth[1]

Received: 31 August 2022 / Accepted: 4 August 2023 / Published online: 16 September 2023

Abstract

Controls on fluid transfer into massive hydraulic fractures are investigated due to reactivation of, and proppant penetration into, oblique fractures transecting the main fracture face during long-term reservoir depletion through tightly constrained laboratory experiments. Permeability evolution of fracture-contained proppant permeability/conductivity is highly sensitive to both normal stress and proppant loading concentration and less sensitive to shear displacement rate. By experimentally examining the shale and steel fractures—as an analog to end-member manifestations of weak/deformable and strong/rigid fracture surfaces—and calibrating using granular mechanics models (DEM), we conclude that the evolution of friction–permeability relationship of a propped shale fracture is largely controlled by the rock friction/rigidity. To be specific, propped strong/rigid fractures show a continuous permeability decay at near-constant rate throughout a shear deformation. Conversely, permeability of weak/deformable fractures declines rapidly during pre-steady-state friction and then declines more slowly after transitioning to steady-state friction. It is posited that weak fracture walls accommodate shear deformation via the combined effects of distributed deformation across the interior of the proppant pack and from sliding at the fracture–proppant interface. However, strong rocks accommodate shear deformation primarily through distributed deformation within the proppant pack.

Highlights

- The permeability of shear-reactivated and propped fractures evolves synchronously with the evolution of friction. Both factors depend on normal stress and proppant loading concentration but are less sensitive to shear displacement rate.
- The degree of permeability reduction decreases with increasing effective normal stress and for samples with thicker proppant packs. Coefficients of friction during steady-sliding decrease as normal stress increases.
- Rock friction/rigidity controls the degree of fracture surfaces damage (as striations or indentations) in shale and consequently impacts the evolution of permeability. Specifically, Strong and rigid fractures show a steady permeability decline during shear deformation, while weak and deformable fractures exhibit a rapid reduction in unsteady-state friction, followed by a slower decline in steady-state friction.
- Weak and deformable fractures accommodate shear deformation via the combined effects of distributed proppant pack deformation and interface sliding, while strong and rigid rocks primarily reply on distributed proppant pack deformation.

Keywords Shale · Propped fracture conductivity

1 Introduction

Recent advances in methods of recovery—horizontal drilling and massive hydraulic fracturing—enable oil and gas recovery from deep, ultralow-permeability shale reservoirs. This new resource has dramatically changed energy supply in the United States and worldwide over the past

✉ Jiayi Yu
jzy200@psu.edu

[1] Department of Energy and Mineral Engineering, EMS Energy Institute and G3 Center, Pennsylvania State University, University Park, PA 16802, USA

[2] Chevron Technical Center, 1500 Louisiana St., Houston, TX 77002, USA

two decades. However, the deployment of massive hydraulic fracturing is accompanied by controversy. Large-scale fluid injection into the subsurface potentially generates overpressure and may result in the reactivation of faults and fractures (Warpinski and Teufei 1987; Maxwell et al. 2009; Zhou et al. 2008; Taleghani and Olson 2011; Zhou and Xue 2011; Taleghani et al. 2016). In addition, the intersection of natural fractures by the driven hydraulic fracture results in complex fracture networks with the architecture controlled by constraints on the crossing of these fractures (Olson and Taleghani 2009; Cheng et al. 2015; Zhang et al. 2017). Oblique fractures intersecting the main hydraulic fracture may reactivate in shear as the effective stress state is modified by the passing hydraulic fracture (Wang et al. 2018). Other plausible causes for fracture slip include stress reorientation and poroelastic effects due to nonuniform pressure depletion in heterogeneous permeability fields (Segall and Fitzgerald 1998; Rousssel and Sharma 2012; Zhang et al. 2017), undesired fluid leakage into pre-existing hydraulic fractures (Guindon 2015), fluid reinjection (Dohmen et al. 2017), and the enhanced interactions between the natural fractures and hydraulic fractures during fracture propagation (Weng 2015; Fang et al. 2017a). Some in situ observations suggest that the induced shear deformations can also influence the fluid transport characteristics of the reservoir formation (Guglielmi et al., 2015). Thus, concurrent observations of shear deformation and fluid transport are important in understanding the evolution of fracture permeability in response to fracture reactivation, especially during long-term reservoir depletion.

Numerous studies address the essential geophysical and geochemical controls on unpropped fractures and their friction–permeability relationships under shear reactivation. The permeability of natural fracture surfaces in contact are known to be strongly stress-, rate- and state dependent in both normal and shear modes of deformation. This includes the impacts of stable versus unstable remobilization (Fang et al. 2017a, 2018), healing, sealing and reactivation (Im et al. 2018), and sorption and desorption of hydrocarbons from organic material (Sang et al. 2017). Theoretical and experimental results on fracture strength as a function of sliding velocity, slip history (state), and effective normal stress demonstrate the important role of asperity contact between the sliding surfaces on strength and stability. The nature, form and rates of fracture healing and concomitant sealing control how the fracture restrengthens and re-fails during the successive fracture preslip–slip cycle (Dieterich 1979; Ruina 1983; Marone 1995; Samuelson et al. 2009; Im et al. 2018). In addition, the evolution of fracture strength and permeability is affected by the combined impact of chemical and mechanical effects that either generates (including dilatant shear, microcracking, thermal cracking, and focused dissolution) or destroys (including shear and hydrostatic compaction, fracture healing, dislocation creep, and pressure solution prompted by water-film and free-face diffusion) porosity.

Similar controls also operate on propped fractures under normal (Kumar et al., 2015; Li et al. 2017) and shear (Zhang et al. 2017) deformations. Additional impacts on the permeability evolution of propped fractures include changes in stress paths during reservoir drawdown (Cikes 2000; Palisch et al. 2007), application of corrosive hydraulic fracturing fluids (Hou et al. 2017; Jia et al. 2018; Wanniarachchi et al. 2018), selection of proppants of different angularities, size distribution, and material (Kurz et al. 2013; Liang et al. 2015) Also impacting permeability is the evolution of the residual propped fracture aperture profile determined by proppant segregation and accumulation (Wang et al. 2018), including during flow-back followed by enhanced rock creep (Zhang et al., 2015) and proppant diagenesis (Lee et al. 2009; Mittal et al. 2018), and as a result of proppant crushing (Zheng and Tannant 2016; Zhang et al. 2017) and embedment (Alramahi et al. 2012) during production. These studies also have explored the impact of proppant loading concentration on the evolution of permeability (Wen et al. 2007; Zhang et al. 2013; Briggs et al. 2014; Elsarawy and Nasr-El-Din, 2018). As such, these studies provide valuable insights into permeability evolution on propped fractures but neglect systematically linking response to friction, stability, and modes of shear reactivation.

This study explores the evolution of friction–permeability relationships in hydraulically fractured and propped shale reservoirs under the combined effects of normal and shear deformations. We accommodate preslip static loading followed by fracture reactivation, which substantially reproduces natural behaviors (Elkhoury et al. 2006; Fang et al., 2018). We define the relative impacts and interactions between specific variables including effective normal stress, shear displacement rate, proppant loading concentration, proppant embedment, and their separate impacts on fluid transport during shear slip. Results are calibrated against granular mechanics (DEM) models to probe controls of rock properties on friction and permeability behaviors. Implications of observed friction–permeability response to the recovery of hydrocarbons from unconventional shale reservoirs are discussed.

2 Experimental Methods

We conduct laboratory experiments reproducing shear reactivation of proppant-filled soft interpenetrated (Marcellus shale) and hard-unpenetrated (steel) fractures. The

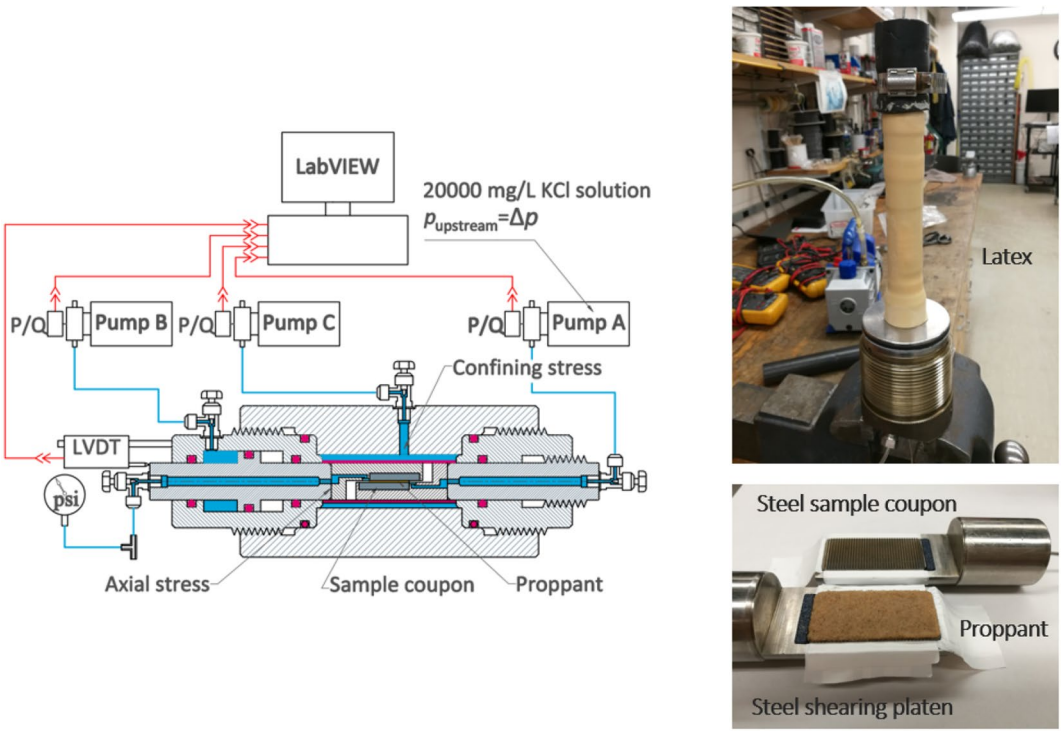

Fig. 1 Direct-shear flow-through apparatus with independent control on confining (pump **C**) and axial (pump **B**) pressures. Upstream flow-through is via pump **A** and discharges downstream to atmospheric pressure. Each sample coupon (bottom right) is constrained within a steel shearing platen. The two coupon halves are positioned face to face with the proppant layer in between (dark yellow), longitudinally offset by ~ 8 mm to allow shear travel. Porous stones are shaped to fit and are positioned at the inlet and outlet of fluid flow (blue frits) to ensure even distribution of fluid, as well as to prevent the proppant particles from being washed out. The assembly is sheathed within a latex membrane (top right) and counter-sheared at a prescribed shear velocity by controlling the flow rate of pump **B** (color figure online)

laboratory fractures are propped by realistic thicknesses (proppant loading concentration) of proppant. Fractures are initially confined at modest normal stresses (σ_n ~ 1–5 MPa) as an analog to a preslip static state, and then sheared at prescribed constant piston/load point velocity to a final shear offset of ~ 5 mm. This allows continuous measurement of evolving frictional strength of the fracture/proppant pack assemblage through the full displacement cycle together with the evolution of fracture conductivity.

2.1 Sample Materials and Preparations

The coupons of Marcellus shale contain (XRD) 43.4% quartz, 46.8% Muscovite, 5.1% Kaolinite and 4.7% Pyrite. The shale samples (38.1 mm × 19.05 mm × 5.08 mm in dimension) are sawcut and then roughened with #360 grit sandpaper to a prescribed and repeatable roughness for all experiments. Coupons made of steel and with identical dimensions are sawcut and grooved on the proppant contacting surface. The grooves are approximately 0.8 mm deep and the distance between adjacent grooves is ~ 1 mm. The grooves run perpendicular to the shear direction and ensure that shear is through the proppant rather than along the proppant–steel interface (Fig. 1). Brine (20,000 mg/L KCl solution) is used as the permeant, representing a typical flow-back water after hydraulic fracturing. The proppant used for this study is 100-mesh sand—a standard material in field production.

2.2 Experimental Setup and Procedures

The friction–permeability experiments are performed in a triaxial testing apparatus with independent control on confining stress (pump C), pore pressure (pump A), and axial stress (pump B). Shear displacement rates are set through the volume rates of pump B and confirmed by a linear variable differential transducer (LVDT) connected to the axial loading piston. The sample coupon twins are housed in a pair of steel shearing platens with proppant sandwiched between them (Fig. 1). A layer of Teflon material is placed between the steel platens and the steel/rock coupon to ensure that the sample is securely held in place. Porous stones are shaped to fit and are positioned at the inlet and outlet of fluid flow (blue frits) to ensure even distribution of fluid throughout the proppant pack, as well

as to prevent the proppant particles from being washed out. The shearing platens are placed face-to-face with the proppant layer sandwiched in between (dark yellow), longitudinally offset by ~ 8 mm and encased within a latex jacket. The jacket functions to isolate and seal the sample assembly from the confining stress. This assembly is then inserted into the pressure vessel (Fig. 1) and the sample sheared by driving the longitudinal shortening of the sample assembly.

The apparatus is pre-calibrated for system resistance by shearing smooth lubricated steel coupon twins—with null friction—and measuring resistance with shear offset. This defines the combined impacts of membrane resistance (of the jacket) and piston-stick to be calibrated out of the resulting data—as reported here.

The experiments follow a hold-then-slide protocol with the hold-period resetting fracture/proppant permeability prior to reactivation a feature shown important in defining permeability evolution (Im et al. 2018). This protocol enables both the separate and combined impacts of static loading and successive shear loading to be determined. Experiments initiate with the application of a confining stress (normal stress in this configuration) retained constant throughout the experiment. The sample is then fluid saturated with brine until the fluid flow stabilizes. After the hold, the hold-then-shear reactivation initiates at a constant prescribed velocity (1–5 µm/s) until a pre-set displacement of ~ 4–4.5 mm is reached. Concurrent fluid flow continues throughout.

Effective stress is defined as the difference between the confining normal stress and pore pressure (Biot coefficient of unity). The pore pressure drop along the fracture is limited to within ~ 1.5% of the confining stress, rendering the effective stress essentially constant. Fluid flow rates are limited to prevent excessive washout of the proppant.

2.3 Pre- and post-experiment analysis

We probe the separate impacts of fracture sorption/swelling and proppant embedment on the permeability evolution of the proppant-filled fracture. Sorption-driven fracture swelling effects reverse as desorption occurs, whereas the plastic damage due to proppant embedment is likely irreversible—thus, they exhibit different signatures to cycled effective stresses. To evaluate the change in fracture surface roughness and topography due to swelling, embedment and the creation of striations during shear slip, fracture surfaces are imaged first before then after the experiments.

Microscopic roughness measurements are conducted on a ZYGO optical surface profilers. Randomly located observation

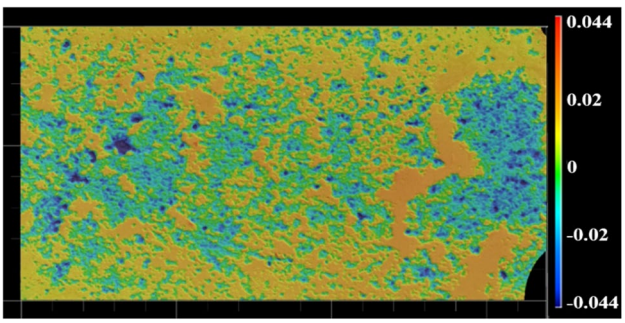

Fig. 3 Example of post-test shale fracture topography showing the entire surface characterized via Keyence VR-3200 optical microscope. The colorbar indicates the elevation differences of peaks and valleys relative to the median surface (colorbar limits: − 0.044 ~ 0.044 mm)

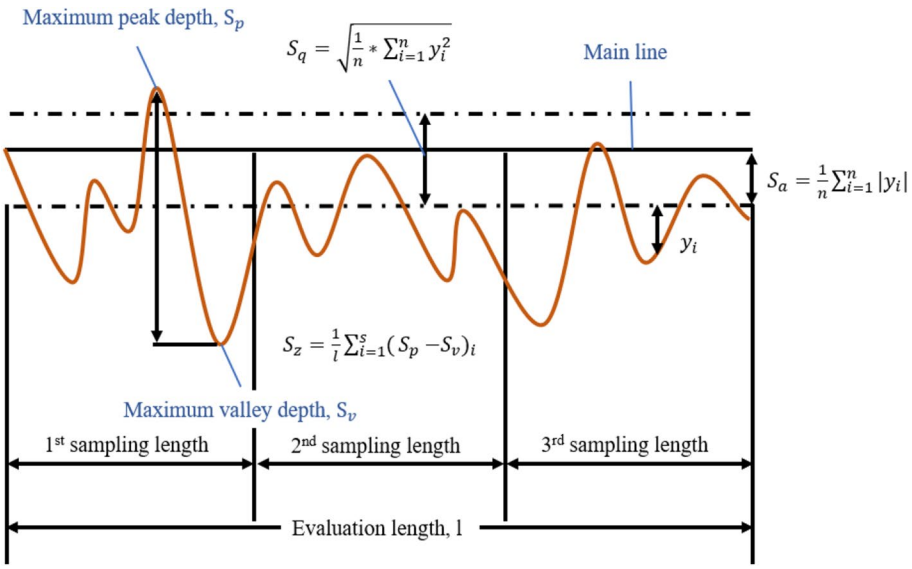

Fig. 2 Surface roughness profile showing select surface roughness parameter indices (Yu et al. 2022)

patches (0.836 mm × 0.836 mm in dimension) are captured from the surface of each specimen and then amalgamated as an ensemble for each fracture surface to define various roughness indices. Surface roughness parameters include the arithmetic mean height of asperities,S_a, the maximum height between peak and valley,S_z, and the root mean square height, S_q, as,

$$S_a = \frac{1}{n}\sum_{i=1}^{n}|y_i|, \tag{1}$$

$$S_z = \frac{1}{l}\sum_{i=1}^{s}(S_p - S_v)_i, \tag{2}$$

$$S_q = \sqrt{\frac{1}{n}\sum_{i=1}^{n} y_i^2}, \tag{3}$$

where the roughness profile (Fig. 2) contains a total of n equally spaced elevations along a section from the 1st to the i_{th} sampled elevation along the trace; y_i is the vertical distance from the mean line to the ith data point; S_p is the maximum peak height; S_v is the maximum valley depth; and l is the sampling length.

Macroscopic roughness measurements are conducted on a Keyence VR-3200 optical microscope (Fig. 3, 19.05 mm × 38.1 mm in dimension). Each image is taken at 80-magnification with a height resolution of 0.1 micron. Roughness measurement is done on a consistent size in the center of the sample with any edge effects from cracks, spalling, or other damage in loading removed. Any long-term dip of the fracture plane is removed from the measurement to eliminate bias in roughness parameters. The colorbar indicates the elevation differences of peaks and valleys relative to the median surface, providing a visual representation of the height variations on a post-test fracture surface. The color range is − 0.044 to 0.044 mm.

2.4 Evaluation of Friction

The ratio of the shear force to the effective normal force indicates a coefficient of friction μ representative of the propped fractures. μ is calculated as a continuous function of shear displacement as the ratio of shear to normal forces applied to the sample as $\mu = F_s/F_n$ and ignoring cohesion,

$$\mu = \frac{F_s}{F_n} = \frac{P_a A_{piston}}{(P_c - P_p)(l - Disp)w}, \tag{4}$$

where P_a[Pa] is the axial loading on the piston, $A_{piston}[m^2]$ is the piston cross sectional area, P_c [Pa] is the confining pressure, P_p[Pa] is the average pore pressure of the saturating fluid (upstream to downstream) along the fracture by assuming a linear pressure distribution, $l[m]$ and $w[m]$ are the length and width of the sample coupon and $Disp[m]$ is the shear displacement.

2.5 Evaluation of Conductivity and Permeability

Conductivity (C) reflects the fluid transmission capability of the entire proppant-filled fracture and is defined based on Darcy's law as

$$C = \frac{\eta(l - Disp)}{w}\frac{Q}{\Delta p}, \tag{5}$$

where η is fluid viscosity (8.9×10^{-4}Pas), Q [m^3/s] is flow rate, and Δp is the difference between the upstream and downstream pore fluid pressures.

The capacity of the proppant pack to transport fluid is characterized by an equivalent propped fracture *permeability* (K), defined as the conductivity (C) normalized by the initial fracture aperture (h). Initial fracture aperture is not measured and is difficult to characterize, but may be approximated as the ratio of proppant bulk density to proppant loading concentration, as

$$K[\mathrm{L}^2] = \frac{C[\mathrm{L}^3]}{h[\mathrm{L}]} = C[\mathrm{L}^3]\frac{\rho_{bulk}[\mathrm{M} * \mathrm{L}^{-3}]}{c_{proppant}[\mathrm{M} * \mathrm{L}^{-2}]}, \tag{6}$$

where ρ_{bulk} is 1630 kg/m^3. Previous studies on fracture aperture evolution vs. effective stress show that fracture aperture is proportional to proppant loading concentration (Fig. 4) (modified from Zhang et al. 2017), suggesting this characterization as useful.

The equivalent permeability defines the transmission effectiveness of the proppant alone and enables direct comparison between experiments with different proppant loading concentrations—highlighting the loss of function of

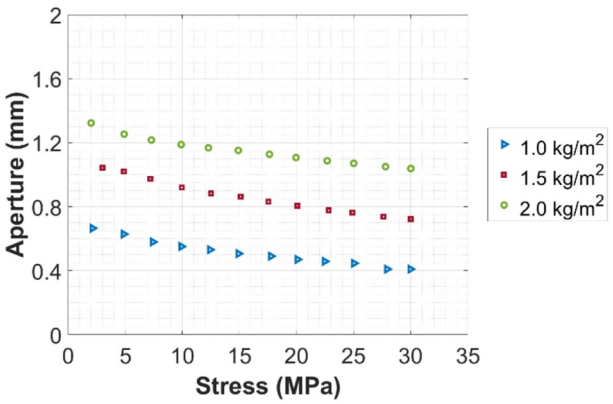

Fig. 4 Experimental results of fracture aperture vs. effective stress for three different proppant loading concentrations with 40/70-mesh proppant (modified from Fig. 4 in Zhang et al. 2017)

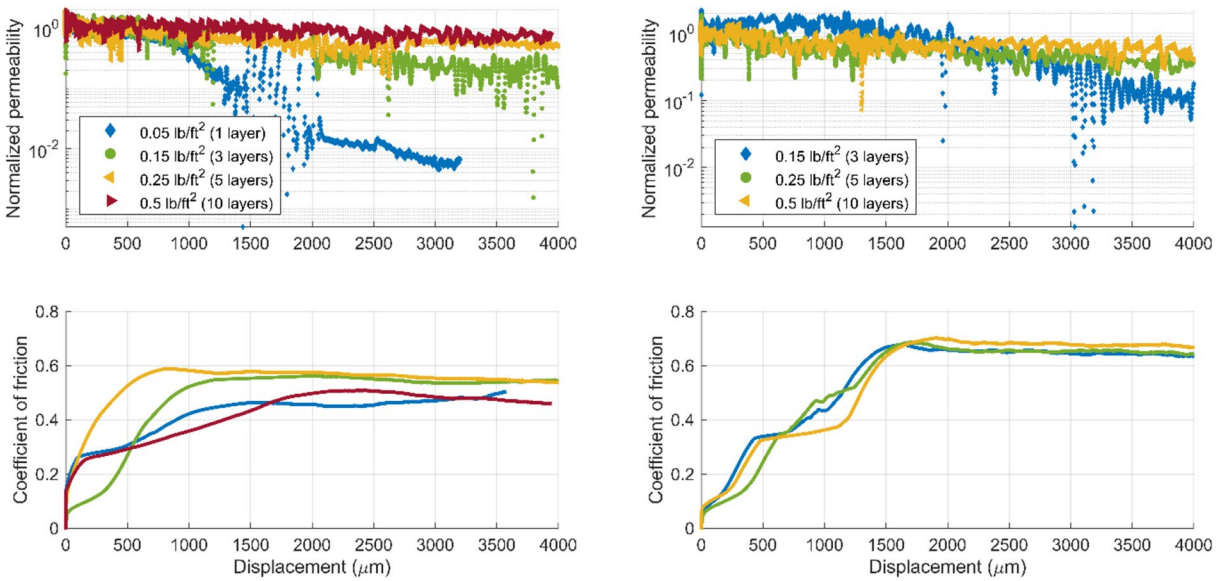

Fig. 5 Evolution of normalized equivalent permeability and friction with respect to shear displacement for shale (left) and steel (right) fractures for a confining stress of 5 MPa and shear rate of 3 μm/s

Table 1 Surface roughness parameters both pre- and post-test for the fracture propped by different numbers of layers of proppant

Sample #	S_a(μm)	S_q(μm)	S_z(μm)
Ground pre-test	0.43	0.56	6.26
Monolayer	11.24	14.18	95.45
3-layer	5.28	6.70	52.09
5-layer	4.80	6.12	49.21
10-layer	4.97	6.07	41.87

Data are obtained via ZYGO optical surface profiler

the proppant itself. However, this parameter assumes that fracture aperture remains constant throughout each experiment. The proppant layer marginally thins with slip and this small error is entrained in the interpretation, impacting the absolute value of permeability but not the trend in response.

3 Results

We evaluate the effects of proppant loading concentration, effective normal stress and shearing velocity on the evolution of friction and permeability of proppant-filled weak/deformable- and strong/rigid-walled fractures. We use these observations to discriminate among key controls on response.

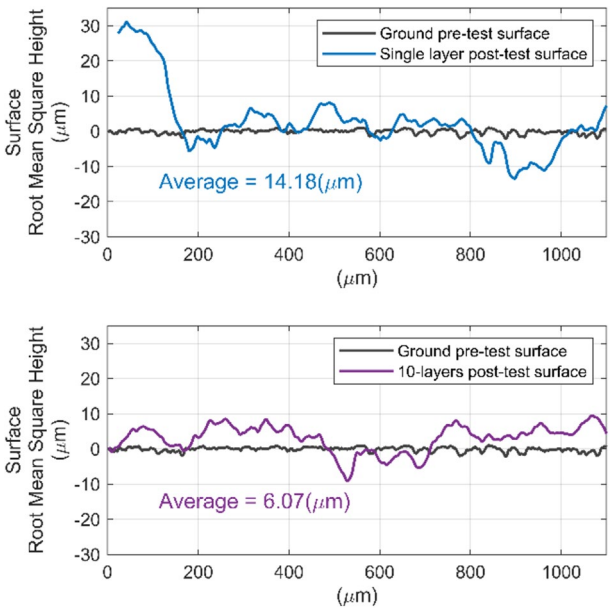

Fig. 6 Comparison of surface height and RMS amplitude S_q between the pristine polished/ground pre-test surface and the post-test fracture propped by different layers of proppant. Data are obtained via ZYGO optical surface profiler

3.1 Effect of Proppant Loading Concentration

Individual fractures contain 100-mesh sand at proppant loading concentrations of 0.05, 0.15, 0.25 and 0.5 lb/ft^2(0.24, 0.73, 1.22 and 2.44 kg/m^2) in successive experiments. A single layer of close-packed proppant weighs ~ 0.18 g therefore these proppant loading

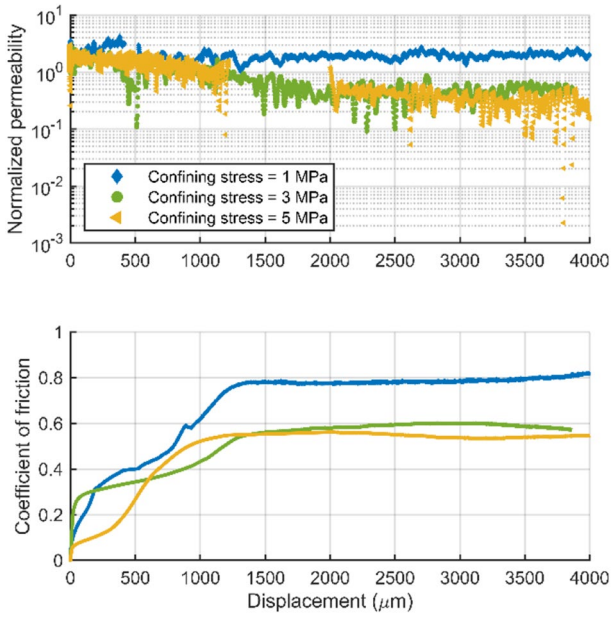

Fig. 7 Evolution of normalized equivalent permeability and friction coefficient as a function of shear displacement. Permeability normalized relative to value at zero shear displacement. Proppant loading concentration is 0.73 kg/m2 (0.15 lb/ft^2) for a shear rate of 3 μm/s

concentrations approximate 1, 3, 5 and 10 layers. Figure 5 shows the evolution of equivalent and normalized equivalent permeability together with friction with shear displacement for both shale (left) and steel (right) fractures at a confining stress of 5 MPa and shear offset rate of 3 μm/s.

For both the Marcellus shale and steel fractures, all experiments exhibit continuous and continuing permeability decay during shearing—presumably due to shear compaction—and independent of whether the fracture walls are deformable or rigid. The relative reduction in permeability decreases with increasing proppant loading concentration—ranging from 50% (10 layers) to 99% (monolayer) for shale—indicating a gradually muted shear sensitivity as proppant pack thickens. This is consistent with observations of the post-test topographies of the shale fracture surfaces (relative to the smoothly ground pre-test surfaces) that proppant embedment, indexed by the surface roughness parameters, is reduced at higher proppant loading concentrations where the resulting post-test surface roughness is flattest (Table 1 and Fig. 6).

However, friction coefficient does not appear to systematically change with proppant loading concentrations.

3.2 Effect of Effective Normal Stress

Figure 7 presents the evolution of normalized equivalent permeability and friction for a suite of experiments on shale fractures propped under different confining stresses ranging from 1 to 5 MPa. The proppant loading concentration for all cases is 0.73 kg/m^2 (0.15 lb/ft^2) and shear rate is 3 μm/s.

Permeability gradually declines during the shearing for all three cases (Fig. 7). The normalized equivalent permeability indicates that the reduction in permeability is most pronounced under the highest normal stress–possibly due to combined action of shear compaction and proppant embedment. At the end of loading, the permeability is

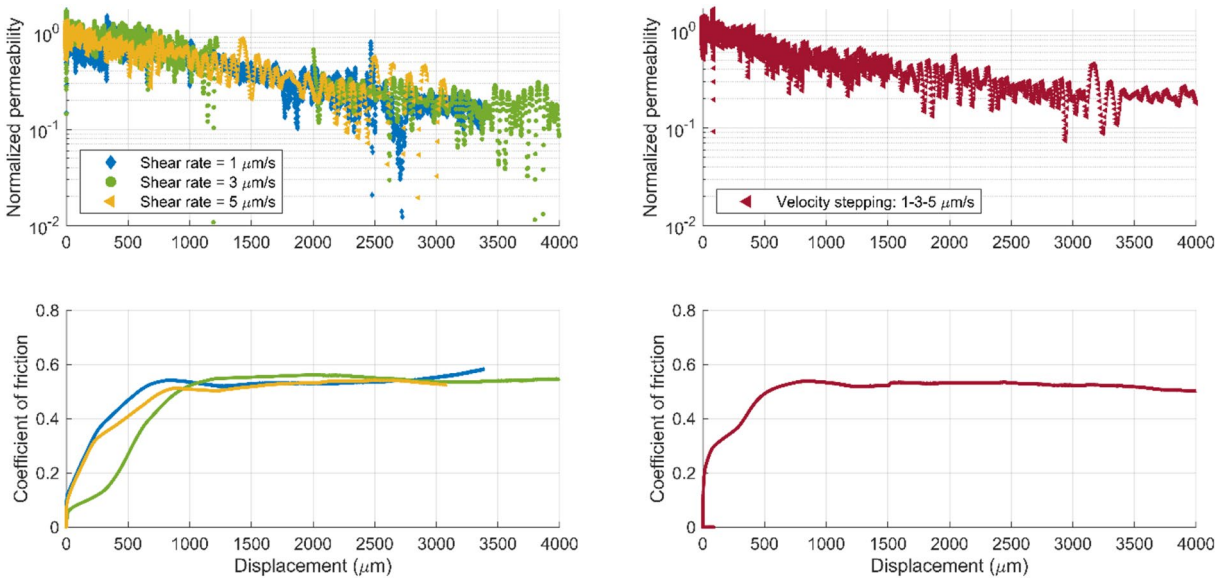

Fig. 8 Evolution of normalized equivalent permeability for constant-shear-velocity (left) and velocity-stepping experiments (right) and friction coefficients as a function of shear displacement. Proppant loading concentration is 0.73 kg/m2 (0.15 lb /ft^2)

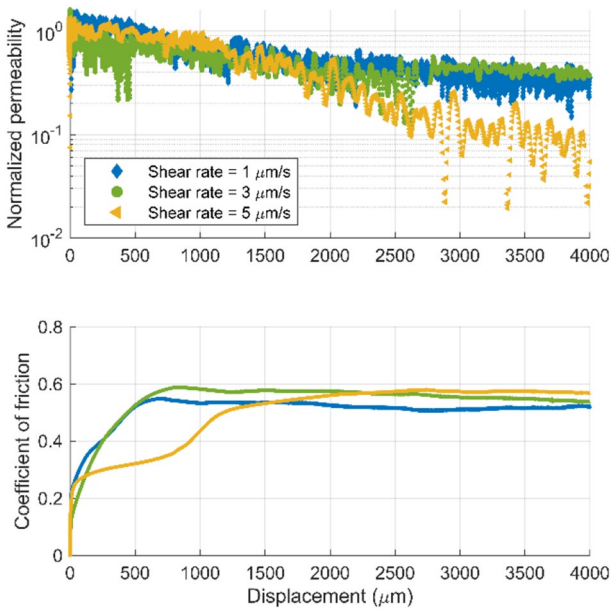

Fig. 9 Evolution of normalized equivalent permeability and friction coefficients as a function of shear displacement. The proppant loading concentration is 1.22 kg/m2 (0.25 lb/ft^2)

unchanged at 1 MPa but reduced by ~ 70–80% at 3–5 MPa, respectively.

The steady-state coefficient of friction decreases as the normal stress increases (Fig. 7). These observations can be attributed to two possible causes. First, at higher normal stresses, the normalized membrane restraint between the sample surface and the membrane is reduced. Therefore, as the normal stress increases, the coefficient of friction converges to the actual value representing the contact behavior between proppant particles and the fracture surface. Second, higher normal stress likely returns the most significant embedment, which potentially changes the contact response at the interface between proppant particles and fracture surfaces.

3.3 Effect of Shear Rate

Permeability reduction and shear strength are both relatively insensitive to shear velocity over the range 1–5 μm/s (Fig. 8a–c). Velocity stepping experiments successively increment shear velocity from 1 to 5 μm/s but show no apparent change in friction as velocity is incremented (apparent from the change in recording frequency of the data apparent in Fig. 8b).

Variable proppant loading concentration experiments conducted with 3-, 5- and 10 layers suggest that this shear-rate insensitivity is broadly independent of proppant loading concentration (Figs. 9, 10 and 11). Furthermore, the transition to steady-state sliding also exhibits a systematic change with proppant loading concentration at 500–1000 μm for 3- and 5 layers to 1500–2000 μm for 10 layers. The implications of this are discussed in Sect. 3.4.

3.4 Effect of Rock Friction/Rigidity

Marcellus shale and steel fractures differ principally in their mechanical characteristics of friction and rigidity. Pervasive

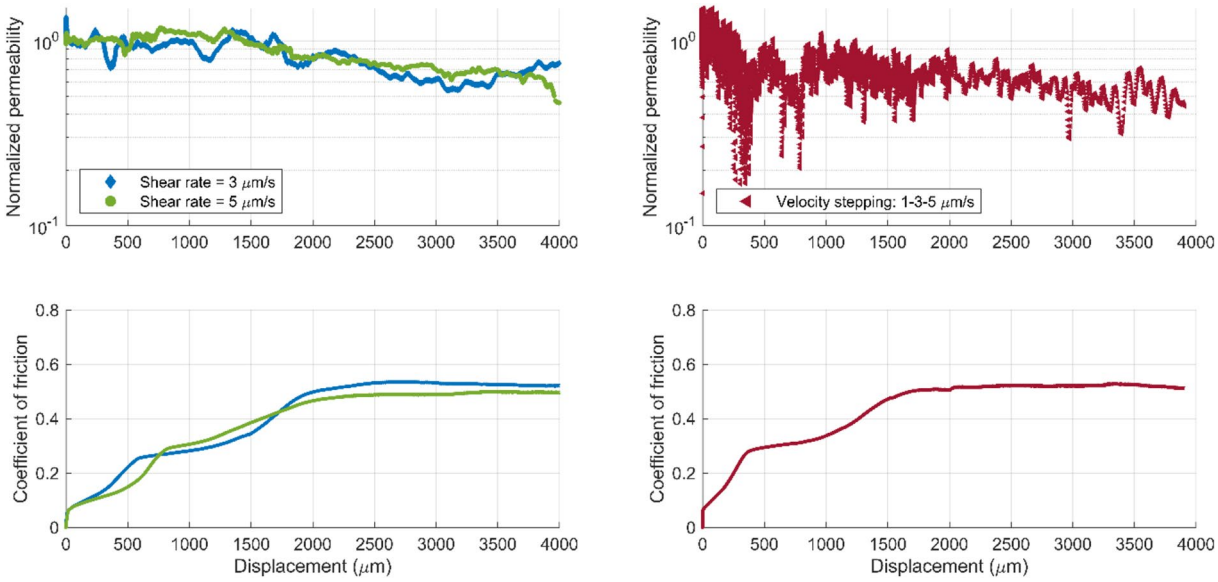

Fig. 10 Evolution of normalized equivalent permeability for constant-shear-velocity (left) and velocity-stepping experiments (right) and friction coefficients as a function of shear displacement. Proppant loading concentration is 2.44 kg/m2 (0.5 l $/ft^2$)

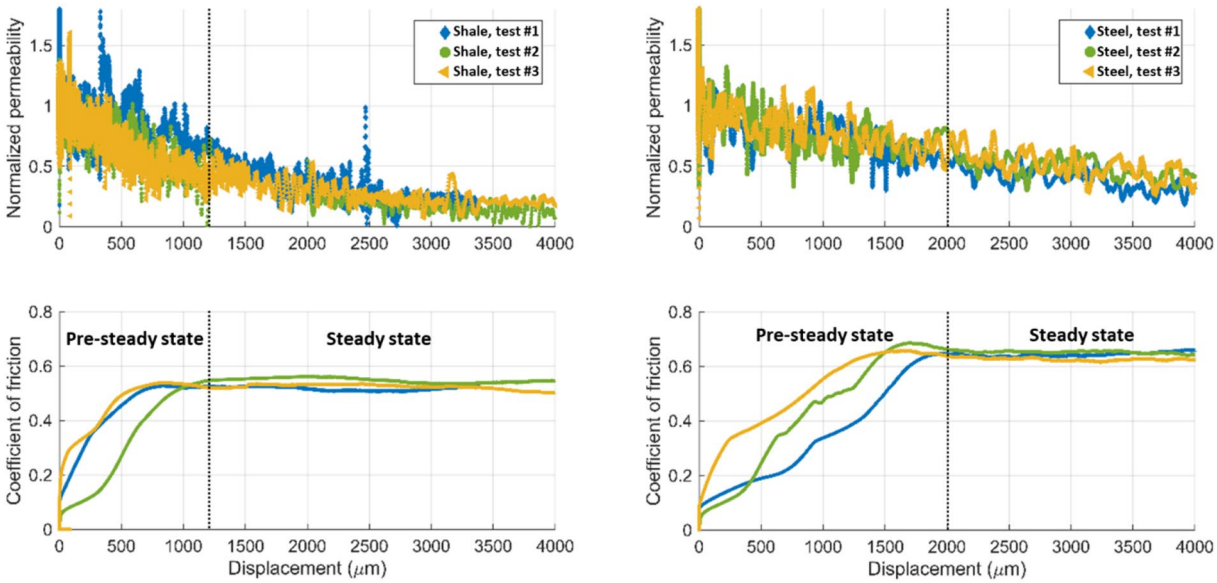

Fig. 11 Representative experimental results showing the evolution of normalized equivalent permeability and friction coefficient as a function of shear displacement, for shale (left) and steel (right) fractures, respectively. The vertical dashed lines indicate the transition of slip mode from pre-steady state to steady state (friction)

damage to the post-test fracture surfaces is observed in the shale due to both proppant embedment then grooving and striating as a result of subsequent slip. However, the steel remains undamaged, thus confirming that the shale and steel represent end-member manifestations of weak/deformable and strong/rigid fracture surfaces. We select three representative experimental results contrasting the response of weak (Marcellus shale; Fig. 11 left) and strong (steel; Fig. 11 right) fracture surfaces to identify key controls.

The evolutions of permeability and friction follow a consistent pattern for each fracture type and do not appear to be impacted by the mass/volume concentration of proppant loading or the rate of shear displacement. The decline in the normalized equivalent permeability of shale fractures is initially rapid. However, once the mode of slip transits to steady-state sliding (denoted by the dashed lines in Fig. 11), the rate of decline in normalized equivalent permeability slows down. In contrast, the normalized equivalent permeability for the steel fractures demonstrates a continuous decay at a nearly constant rate with respect to shear displacement for the full duration of shear. This decay is broadly independent of the mode of slip, whether it occurs before or after reaching a steady-state condition.

There are two modes in which deformation takes place in the proppant–fracture assemblage. Before failure, the quasi-elastic shear deformation features a linear relationship with both the thickness of the proppant and the shear stress before failure. After failure, the deformation will be continuous occurring under the constant peak shear stress, where the slips can occur between the proppant and the fracture

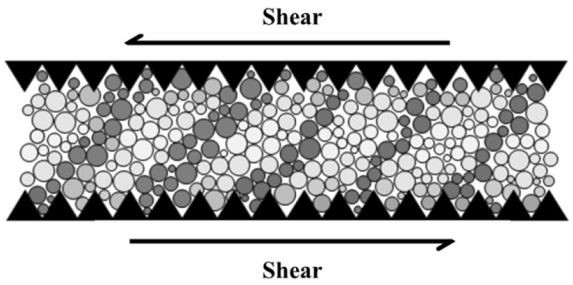

Fig. 12 Schematic diagrams of proppant particles sheared rough steel fracture boundaries. A layer of grains is contained along the bounding surface and allow slip to localize along shear band adjacent to this layer. Particles form force chains that are inclined about 45° to the shear zone walls (modified from Fig. 10a in Mair et al., 2002)

wall, as wells as within the proppant itself—sliding against each other. The shear displacement marking the transition to steady-state friction (Sect. 3.3) is broadly proportional to the proppant loading concentration. This suggests that in unsteady-state friction (preceding steady-state) the proppant pack rearranges to a denser packing—accommodating the shear strain through internal deformation. The transition to steady-state friction occurs as the proppant–wall interface is mobilized by localizing slip—suggested by the presence

of striations along the fracture wall where this transition has occurred, and absent where it has not. Conversely, for proppant directly contacting steel, grain-to-grain sliding is the cardinal mode of deformation, as the roughened and frictionally locked fracture surface promotes shearing that is distributed throughout the proppant pack. Force chains will develop throughout the particulate pack and spawn shear zones inclined at ~ 45° to the fracture walls (Sammis et al., 1986; Liu et al., 1995; Cates et al., 1998; Aharonov and Sparks, 1999; Morgan and Boettcher, 1999; Albert et al., 2001; Anthony and Marone, 2004). Figure 12 shows a schematic with a layer of grains along the bounding wall (light gray) that act with a bridge of particles that constitute a force chain (dark gray) with intermediate spectator grains (white) that carry little to no load. The forces chains support the load but intermittently become misaligned, buckle, and fail then immediately reorganize into a new configuration of force chains. Angular particles form force chains that evolve subtly but continuously during shear, resulting in a dynamic equilibrium (stabilized shear deformation denoted by the constant coefficient of friction), which agrees with our observations (Fig. 11c and b) (Anthony and Marone, 2005).

Coefficients of friction during steady sliding are different for shale and steel as $\mu = 0.5$ for Marcellus shale and 0.65 for steel fractures. This is also consistent with our hypothesis that steel fractures accommodate shear strain primarily by particle dilation, and the associated interparticle interlocking and jamming increase the bulk frictional resistance. Shale fractures on the other hand accommodate strain by shearing along the surfaces, in which the interior structure of the proppant pack is relatively stable and results in a lower frictional strength.

4 Discussion

Our laboratory experiments reveal that permeability evolution of propped fractures is controlled by the evolution of friction—mechanisms of deformation both pre- and post-steady-state friction control permeability. Thus, permeability evolves synchronously with friction and both correlations are strongly dependent on normal stress and proppant loading concentration. Rock strength, which is referred here as the yield strength of a fracture where fracture surfaces deform plastically to accommodate proppant embedment, is additionally observed to exert control on this relationship. Propped strong fractures (steel) show a continuous decay in permeability at near-constant rate throughout a shear deformation. Conversely, permeability of weak fractures (Marcellus shale) declines rapidly during unsteady-state friction that declines more slowly after transitioning to steady-state friction. We posit that weak fracture walls accommodate shear deformation via the combined effects of distributed deformation across the interior of the proppant pack and from sliding

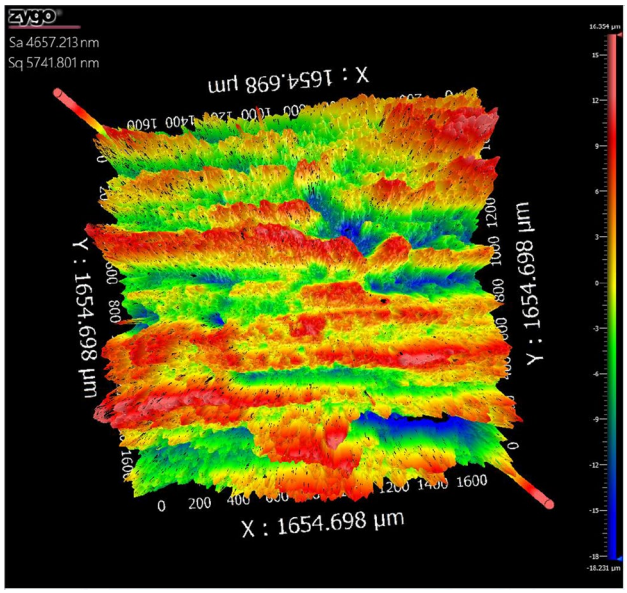

Fig. 13 Microscale fracture topographies characterized via white light optical profilometry for post-test fracture surface

at the fracture–proppant interface. Conversely, strong rocks accommodate shear deformation primarily through distributed deformation within the proppant pack. This conjecture is supported by the fusion of observed changes in surface topography of the samples with the results of simulations using granular mechanics models (DEM).

4.1 Change in Surface Topography Due to Fracture Shearing

Figure 13 shows the surface scanning results of the post-shear Marcellus shale fractures via white light optical profilometry. The sample is dimpled from proppant embedment with prominent shear-induced striations oriented in the direction of fracture shearing (Fig. 13).

The absence of striations on the post-test Marcellus shale fractures that did not undergo shear deformation (Fig. 3) indicates that the sliding of proppant along the fracture wall is an important factor.

4.2 Numerical Modeling of Propped Fracture Shear Deformation

The suggested linkage between modes of deformation and evolution of permeability noted previously may be tested through the application of mechanics-based models. We developed a model via Particle Flow Code 2D (PFC2D) utilizing the principles of Discrete Element Method (DEM). Circular particles to represent both the fracture (as bonded

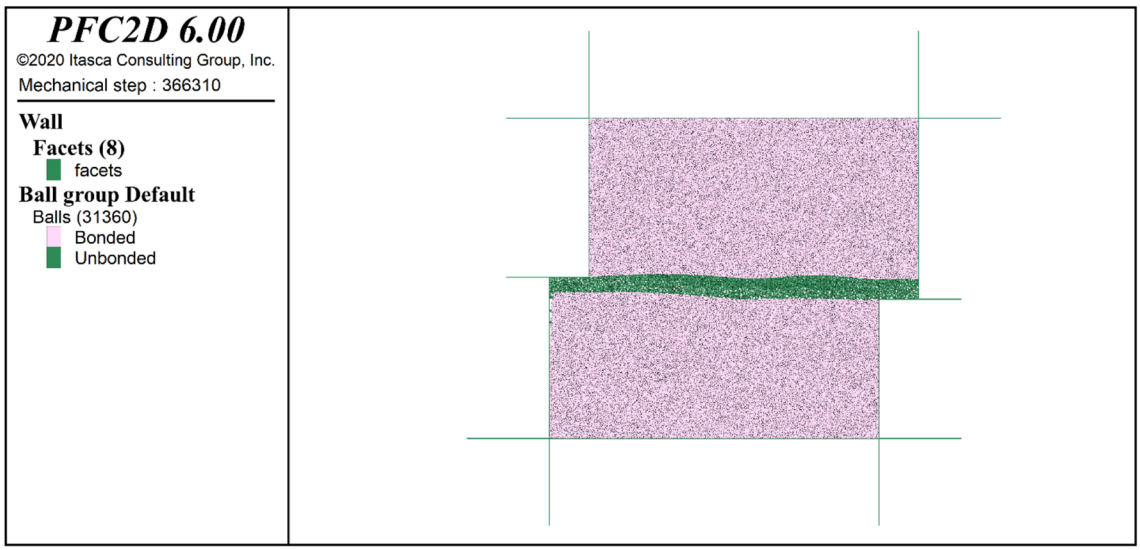

Fig. 14 DEM model configuration as an analog of a single direction shear. A proppant pack of realistic loading concentrations (green) is sandwiched between fractures (pink). A linear elastic contact model is implemented to proppant particles, while a linear parallel-bond model is implemented for fracture rock particles (color figure online)

Table 2 Model parameters for shale rock and proppant analogs

	Shale analog	Proppant analog	Unit
Density	2650	2650	kg/m^3
Interparticle friction	0.6	0.6	NA
Effective modulus	4.2×10^8	13×10^8–13×10^9	N/m^2
Normal-to-shear stiffness ratio	1.5	1.5	NA
Cohesion	1.5×10^6–15×10^6	NA	Pa
Tensile strength	1.5×10^6–15×10^6	NA	Pa

particles) and proppant pack. Such granular mechanics models are capable of representing the key features of proppant fracture systems but simplify in neglecting the role of angularity and out-of-plane rotations in representing the real physical response. A schematic model is shown in Fig. 14, with the relevant parameters and values defined in Table 2.

The fracture–proppant assemblage is represented by a layer of unbonded particles (proppant) sandwiched between two blocks of bonded particles (rock) (Fig. 14). For the purpose of simplification, we opted to use a uniform particle size distribution for all model components. The particle size chosen was small enough to capture the interactions but not so small as to compromise the computational efficiency. The system is initially pre-consolidated at a constant confining stress, with shear then actuated by assigning the upper shear platen with a prescribed velocity while holding the lower shear platen static. Experimental parameters are recorded until a pre-set shear displacement is reached. A linear elastic contact model is implemented at grain–grain contacts for proppant particles (green particles in Fig. 14). The rock sandwiching the proppant is represented by a linear parallel-bond model (pink particles in Fig. 14). The linear elastic contact model does not resist relative rotation, and slip is accommodated by imposing a Coulomb limit on the shear force. The parallel-bond model, in contrast, resists relative rotation when the interface is bonded, with linear elastic response until the strength limit is exceeded and the bond breaks. The material and contact parameters are calibrated using virtual biaxial compression and tension experiments on unbonded (proppant) and bonded (shale) analogs and comparing against laboratory data.

Via this model, we discuss the influence of rock strength by varying the tensile strength and cohesion for the contacts while keeping other parameters on the friction–permeability response under shear deformation. Shear reactivation of granular fault gouge (an analog to proppant) is accompanied by dilation or compaction—representing a mechanism through which deformation may impact permeability via changes in porosity and related permeability (Wang et al. 2017). This represents a causal link between shear reactivation-related deformations and permeability. Figure 15 shows the results of a representative simulation as evolution of the

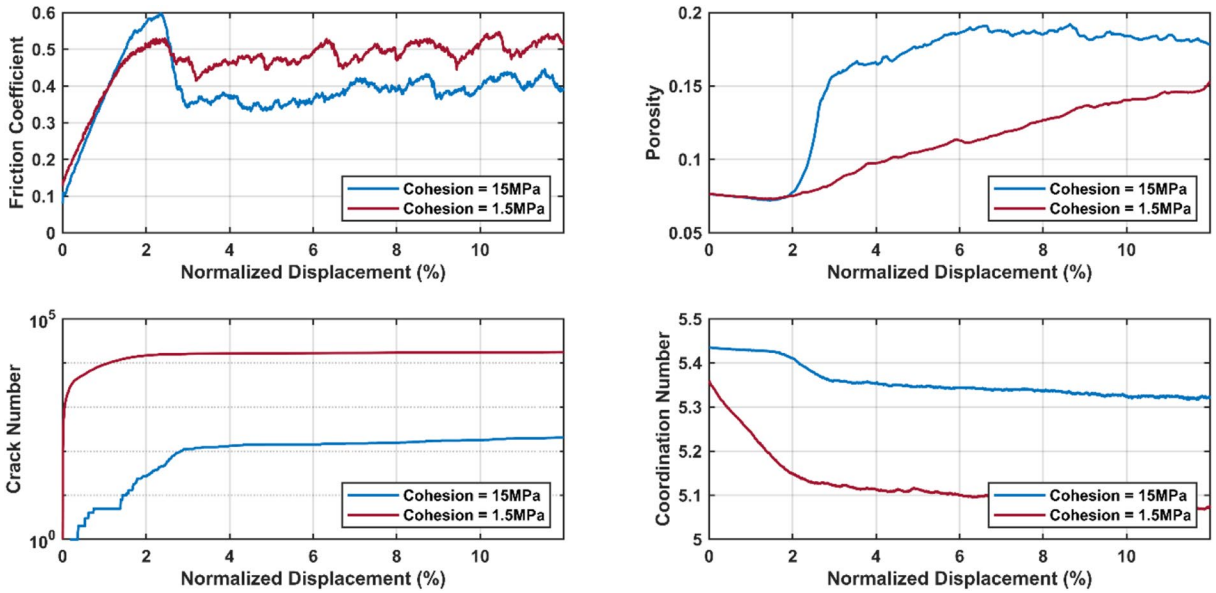

Fig. 15 Evolutions of coefficient of friction, crack number, porosity, and coordination number for propped fractures during hold-slide experiments, respectively, for strong rock (high rock strength) and weak rock (low rock strength)

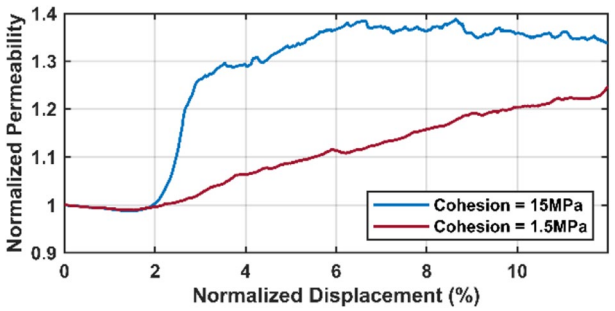

Fig. 16 Evolutions of normalized equivalent permeability with respect to the initial value at displacement zero, respectively, for strong rock (high rock strength) and weak rock (low rock strength)

coefficient of friction, crack number, porosity, coordination number and normalized equivalent permeability for a hold-slide experiment. The evolution of porosity together with the coordination number (average number of contacts around a particle) indicates a potential dilation or compaction at grain–grain scale.

Both materials show an initial reduction in porosity, when compaction-induced porosity loss dominates over porosity enhancement due to shear dilation—occurring before shear deformation is mobilized (normalized displacement of ~ 1.5%). The strong/rigid fracture resists particle self-rearrangement during initial dynamic shearing, promoting dilation and resulting in a rapid increase in porosity. The shear deformation then reaches a dynamic equilibrium (steady-state friction) during which porosity no longer increases. This may be explained by the generation and breakage of force chains, as the strong fracture wall accommodates strain primarily by particle rearrangement. The weak/deformable fracture accommodates strain primarily by breaking particle bonds and by rearrangement of the bond-broken particles damaged in the fracture interface (i.e., crack number). With the continuous 'spalling' of particles from the fracture surface, an additional deformation degree of freedom is added to the system and fracture porosity exhibits a synchronous increase. Estimates of permeability evolution shown in Fig. 16 are calculated from (Wang et al., 2016),

$$\frac{k}{k_0} \cong \left(1 + \frac{\Delta H}{H}\right)^3, \tag{7}$$

$$\frac{\Delta H}{H} \cong \Delta\phi, \tag{8}$$

where k/k_0 is the permeability normalized relative to the initial permeability, k_0, ΔH/H is the change in fracture thickness relative to the original thickness, and $\Delta\phi$ is the relative difference in porosity (Wang et al., 2016). In the absence of grain breakage, permeability evolution is primarily controlled by changes in proppant pack porosity via compaction or dilation. This does not incorporate other possible permeability impairing mechanisms such as proppant embedment and crushing. This explains the disparities between laboratory measurements and numerical modeling results, as the

former shows a decrease in permeability that is largely not present in the latter.

5 Conclusion

Concurrent shear-flow-through experiments are conducted on propped fractures of Marcellus shale to understand the evolution of permeability and its systematic linkage to friction, stability and modes of shear reactivation. It is apparent that:

1) The permeability of shear-reactivated and propped fractures evolves synchronously with the evolution of friction. Both friction and permeability are strongly dependent on normal stress and proppant loading concentration but less sensitive to shear displacement rate.
2) The degree of permeability reduction decreases with increasing effective normal stress and for samples with thicker proppant packs. Coefficients of friction during steady sliding decrease as normal stress increases.

Post-test observations of the topography of both shale and steel fractures are used as an analog to end-member manifestations of weak/deformable and strong/rigid fracture surfaces and show that:

3) Rock friction/rigidity controls on the evolution damage on the fracture surfaces (as striations or indentations) in shale and significantly and systematically impacts the evolution of permeability. Specifically, propped strong/rigid fractures (steel) show a continuous decay in permeability at near-constant rate throughout applied shear deformation. Conversely, the permeability of propped weak/deformable fractures (Marcellus shale) declines rapidly during unsteady-state friction that declines more slowly after transitioning to steady-state friction.

Characterizations of surface topography coupled with granular mechanics modeling (DEM) suggest that:

4) Weak/deformable fracture walls accommodate shear deformation via the combined effects of distributed deformation across the interior of the proppant pack and from sliding at the fracture–proppant interface. Conversely, strong/rigid rocks accommodate shear deformation primarily through distributed deformation within the proppant pack.

This study provides insight into the combined effect of preslip static loading followed by fracture reactivation on the fluid transport characteristics of propped fractures in shale reservoirs. These results emphasize the significant impact of friction–permeability relationship on the transmission characteristics of off-fracture features during hydraulic fracturing and the combined role of proppant density and shale fracture wall characteristics.

Acknowledgements This work was supported by Chevron ETC. This support is gratefully acknowledged.

Data Availability Statement Due to the sensitive nature of the research, the supporting data for this study is not available for public access or sharing.

Declarations

Conflict of Interest The authors declare that they have no conflicts of interest.

References

Alramahi B, Sundberg MI (2012) Proppant embedment and conductivity of hydraulic fractures in shales. In: 46th US rock mechanics/geomechanics symposium. OnePetro

Briggs K, Hill AD, Zhu D, Olson K (2014) The relationship between rock properties and fracture conductivity in the Fayetteville Shale. In: SPE Annual Technical Conference and Exhibition. OnePetro

Cheng W, Jin Y, Chen M (2015) Reactivation mechanism of natural fractures by hydraulic fracturing in naturally fractured shale reservoirs. J Nat Gas Sci Eng 23:431–439

Cikes M (2000) Long-term hydraulic-fracture conductivities under extreme conditions. SPE Prod Facil 15(04):255–261

Dahi-Taleghani A, Olson JE (2011) Numerical modeling of multistranded-hydraulic-fracture propagation: accounting for the interaction between induced and natural fractures. SPE J 16(03):575–581

Dieterich JH (1978) Time-dependent friction and the mechanics of stick-slip. In: Rock friction and earthquake prediction (pp. 790–806). Birkhäuser, Basel

Dohmen T, Zhang J, Barker L, Blangy JP (2017) Microseismic magnitudes and *b*-values for delineating hydraulic fracturing and depletion. SPE J 22(05):1624–1634

Elsarawy Ahmed M, Hisham A, Nasr-El-Din (2018) "Proppant performance in marcellus shale fractures under experimental in-situ stress conditions." SPE/IADC Middle East Drilling Technology Conference and Exhibition. OnePetro, 2018

Fang Y, Wang C, Elsworth D, Ishibashi T (2017a) Seismicity-permeability coupling in the behavior of gas shales, CO2 storage and deep geothermal energy. Geomech Geophys Geo-Energy Geo-Res 3(2):189–198

Fang Y, Elsworth D, Wang C, Ishibashi T, Fitts JP (2017b) Frictional stability-permeability relationships for fractures in shales. J Geophys Res Solid Earth 122(3):1760–1776

Fang Y et al (2018) Mineralogical controls on frictional strength, stability, and shear permeability evolution of fractures. J Geophys Res Solid Earth 123(5):3549–3563

Guindon L (2015) Determining interwell connectivity and reservoir complexity through fracturing pressure hits and production-interference analysis. J Can Pet Technol 54(02):088–091

Hou P, Gao F, Ju Y, Yang Y, Gao Y, Liu J (2017) Effect of water and nitrogen fracturing fluids on initiation and extension of fracture in hydraulic fracturing of porous rock. J Nat Gas Sci Eng 45:38–52

Im K, Elsworth D, Fang Y (2018) The influence of preslip sealing on the permeability evolution of fractures and faults. Geophys Res Lett 45(1):166–175

Jia Y, Lu Y, Elsworth D, Fang Y, Tang J (2018) Surface characteristics and permeability enhancement of shale fractures due to water and supercritical carbon dioxide fracturing. J Petrol Sci Eng 165:284–297

Kurz B, Darren Schmidt PE, Cortese P (2013) Investigation of improved conductivity and proppant applications in the Bakken formation. In: SPE Hydraulic Fracturing Technology Conference. OnePetro.

Lee DS, Elsworth D, Yasuhara H, Weaver JD, Rickman R (2010) Experiment and modeling to evaluate the effects of proppant-pack diagenesis on fracture treatments. J Petrol Sci Eng 74(1–2):67–76

Li X, Feng Z, Han G, Elsworth D, Marone C, Saffer D, Cheon DS (2017) Permeability evolution of propped artificial fractures in Green River shale. Rock Mech Rock Eng 50(6):1473–1485

Liang F, Sayed M, Al-Muntasheri G, Chang FF (2015)\ Overview of existing proppant technologies and challenges. In: SPE Middle East Oil & Gas Show and Conference. OnePetro

Marone C (1995) Fault zone strength and failure criteria. Geophys Res Lett 22(6):723–726

Maxwell SC, Waltman C, Warpinski NR, Mayerhofer MJ, Boroumand N (2009) Imaging seismic deformation induced by hydraulic fracture complexity. SPE Reservoir Eval Eng 12(01):48–52

Mittal A, Rai CS, Sondergeld CH (2018) Proppant-conductivity testing under simulated reservoir conditions: impact of crushing, embedment, and diagenesis on long-term production in shales. SPE J 23(04):1304–1315

Olson JE, Taleghani AD (2009) Modeling simultaneous growth of multiple hydraulic ractures and their interaction with natural fractures. In: SPE hydraulic fracturing technology conference. OnePetro

Palisch TT, Duenckel RJ, Bazan LW, Heidt JH. Turk GA (2007) Determining realistic fracture conductivity and understanding its impact on well performance-theory and field examples. In: SPE Hydraulic Fracturing Technology Conference. OnePetro.

Roussel NP, Sharma MM (2012) Role of stress reorientation in the success of refracture treatments in tight gas sands. SPE Prod Oper 27(04):346–355

Samuelson J, Elsworth D, Marone C (2009) Shear-induced dilatancy of fluid-saturated faults: Experiment and theory. Journal of Geophysical Research: Solid Earth

Sang G, Elsworth D, Liu S, Harpalani S (2017) Characterization of swelling modulus and effective stress coefficient accommodating sorption-induced swelling in coal. Energy Fuels 31(9):8843–8851

Segall P, Fitzgerald SD (1998) A note on induced stress changes in hydrocarbon and geothermal reservoirs. Tectonophysics 289(1–3):117–128

Taleghani AD, Gonzalez M, Shojaei A (2016) Overview of numerical models for interactions between hydraulic fractures and natural fractures: challenges and limitations. Comput Geotech 71:361–368

Wang J, Elsworth D (2018) Role of proppant distribution on the evolution of hydraulic fracture conductivity. J Petrol Sci Eng 166:249–262

Wang J, Elsworth D, Denison MK (2018) Hydraulic fracturing with leakoff in a pressure-sensitive dual porosity medium. Int J Rock Mech Min Sci 107:55–68

Wanniarachchi WAM, Ranjith PG, Perera MSA, Rathnaweera TD, Zhang DC, Zhang C (2018) Investigation of effects of fracturing fluid on hydraulic fracturing and fracture permeability of reservoir rocks: an experimental study using water and foam fracturing. Eng Fract Mech 194:117–135

Warpinski NR, Teufel LW (1987) Influence of geologic discontinuities on hydraulic fracture propagation (includes associated papers 17011 and 17074). J Petrol Technol 39(02):209–220

Wen Q, Zhang S, Wang L, Liu Y, Li X (2007) The effect of proppant embedment upon the long-term conductivity of fractures. J Petrol Sci Eng 55(3–4):221–227

Weng X (2015) Modeling of complex hydraulic fractures in naturally fractured formation. J Unconvent Oil Gas Res 9:114–135

Yu J, Wang J, Wang S, Li Y, Singh A, Rijken P, Elsworth D (2022) Conductivity Evolution in Propped Fractures During Reservoir Drawdown. Rock Mechanics and Rock Engineering, 1–15.

Zhang J, Kamenov A, Zhu D, Hill AD (2013) Laboratory measurement of hydraulic fracture conductivities in the Barnett shale. In: SPE Hydraulic Fracturing Technology Conference. OnePetro.

Zhang, F., Fang, Y., Elsworth, D., Wang, C., & Yang, X. (2017). Evolution of friction and permeability in a propped fracture under shear. Geofluids, 2017

Zheng W, Tannant D (2016) Frac sand crushing characteristics and morphology changes under high compressive stress and implications for sand pack permeability. Can Geotech J 53(9):1412–1423

Zhou J, Chen M, Jin Y, Zhang GQ (2008) Analysis of fracture propagation behavior and fracture geometry using a tri-axial fracturing system in naturally fractured reservoirs. Int J Rock Mech Min Sci 45(7):1143–1152

Zhou J, Xue C (2011) Experimental investigation of fracture interaction between natural fractures and hydraulic fracture in naturally fractured reservoirs. In; SPE Europec/Eage Annual Conference and Exhibition. OnePetro.